RSC Advances

PAPER

View Article Online
View Journal | View Issue

Cite this: *RSC Adv.*, 2023, **13**, 5249

A chiral magnetic molybdenum disulfide nanocomposite for direct enantioseparation of *RS*-propranolol†

Hai-Rong Yu, ‡[ab] Li Lei, ‡[a] Yan-Lin Wang, [a] Xi Wang, [a] Ting Liang *[ab] and Chang-Jing Cheng *[ab]

We herein report a novel chiral magnetic molybdenum disulfide nanocomposite ($MMoS_2$/PNG-CD) with a high enantioselectivity and excellent thermosensitivity and magnetism. The prepared $MMoS_2$/PNG-CD shows temperature-dependent chiral discrimination and enantioselectivity toward a chiral drug *RS*-propranolol (*RS*-PPL), which is based on the molecular recognition ability of beta-cyclodextrin (β-CD) and the thermosensitivity of poly(*N*-isopropylacrylamide) (PNIPAM). The synthesized $MMoS_2$/PNG2-CD by using a monomer molar ratio of GMA to NIPAM of 2 : 1 demonstrates a high selectivity toward *R*-PPL over *S*-PPL due to the synergistic effect of the PNIPAM moieties and β-CD hosts. The thermo-induced volume phase transition (VPT) of the introduced PNIPAM moieties significantly affects the inclusion constants of the β-CD/*R*-PPL complex, and thus the loading and desorption of *R*-PPL on the $MMoS_2$/PNG2-CD. The enantioselectivity at temperatures below the lower critical solution temperature (LCST) of the PNG-β-CD grafting chains is much higher than that at temperatures above the LCST. As a result, the regeneration of the $MMoS_2$/PNG2-CD is easily achieved *via* simply changing the operating temperature. Moreover, the regenerated $MMoS_2$/PNG2-CD can be readily recovered from the *RS*-PPL solution under an external magnetic field for reuse. Such a multifunctional molybdenum disulfide nanocomposite with a high enantioselectivity and excellent thermosensitivity and regenerability is promising to serve as a high-performance nanoselector for direct resolution of various β-blocker drugs.

Received 5th August 2022
Accepted 16th January 2023

DOI: 10.1039/d2ra04866c

rsc.li/rsc-advances

1. Introduction

Chiral recognition and enantioseparation of molecules play important roles in numerous fields, such as medicines, synthetic chemistry, food additives, and agrochemicals.[1–3] Individual enantiomers of chiral drugs usually exhibit significantly different pharmacological activities, toxicities, metabolic effects and rates due to the high degree of stereoselectivity of enzymatic reactions and other biological processes.[4,5] β-Adrenergic blocking agents (β-blockers), as a type of representative chiral drugs, are widely used for the treatment of angina, cardiac arrhythmias, hypertension, myocardial infarction and glaucoma.[6–9] They are commonly marketed and administered as racemic mixtures. The pharmacological activities usually reside in the *S*-enantiomer owing to its higher stereoselective affinity toward β-receptors, while the *R*-enantiomer is pharmacologically inactive or even toxic in some cases.[6–8] *RS*-Propranolol (*RS*-PPL), as an important β-blocker, is extensively utilized in treating cardiovascular diseases, such as angina pectoris, arrhythmia, myocardial infarction, and dysfunctional labor and anxiety.[8,9] But the two isomers of PPL usually show significantly distinct pharmacodynamics and pharmacokinetics. For example, the metabolism and elimination of *S*-PPL is faster than those of *R*-PPL, and the activity of *S*-PPL is 100 times higher than that of the *R*-PPL since the β-blocker activity relies on the *S*-enantiomer.[8,9] Hence, effective identification and resolution of *RS*-PPL to obtain single isomers is of importance and highly desirable. To date, various techniques have been developed for the enantioseparation of β-blockers including high-performance liquid chromatography (HPLC),[6,9,10] gas chromatography (GC),[11] thin layer chromatography (TLC),[12] capillary electrochromatography (CEC),[13,14] and capillary electrophoresis (CE).[15–17] However, they are generally laborious, high cost and complicated in operation, thus hampering their practical applications. By contrast, direct resolution of *RS*-PPL by using chiral magnetic nanoselectors (CMNSs) is a feasible strategy to obtain single isomers due to its simplicity in operation, inexpensiveness, and easy manipulation.[18–22] The key of this method is to develop high-performance CMNSs.

[a]*College of Chemistry and Environment, Southwest Minzu University, Chengdu, Sichuan, 610041, China. E-mail: liangting@swun.edu.cn; chengcj@swun.edu.cn*

[b]*Key Laboratory of Pollution Control Chemistry and Environmental Functional Materials for Qinghai-Tibet Plateau of the National Ethnic Affairs Commission, College of Chemistry and Environment, Southwest Minzu University, Chengdu, Sichuan, 610041, China*

† Electronic supplementary information (ESI) available. See DOI: https://doi.org/10.1039/d2ra04866c

‡ Those authors contributed equally to this work.

The currently existing CMNSs obtained mainly *via* surface modification of magnetic nanomaterials using various chiral molecules or materials, such as lipases,[23] polynorepinephrine,[7] cellulose,[24] bovine serum albumin (BSA),[25] chiral metal organic frameworks (MOFs),[26] and β-cyclodextrin (β-CD) and its derivatives.[27,28] Those CMNSs have been widely verified to own high enantioselectivity toward a variety of enantiomeric compounds. However, organic solvents or inorganic salts are required to release the loaded enantiomers from those CMNSs to realize the regeneration of the nanoselectors, which seems to be complicated and environmentally unfriendly.[18–20,22,29–31] Poly(*N*-isopropylacrylamide) (PNIPAM) is a popular smart polymer that can occur reversible volume phase transition (VPT) in water as the surrounding temperature changes across its lower critical solution temperature (LCST) of ~32 °C, thus showing excellent thermosensitivity.[32] β-CD is a cyclic polysaccharide and consists of seven glucose units characteristic of a hydrophobic cavity, in which a large number of guests can be loaded to form inclusion complexes based on van der Waals forces, hydrophobic interactions, hydrogen bonding interactions,[33] hence demonstrating high chiral discrimination and enantioselectivity. Besides, the incorporation of β-CD into PNIPAM chains allows the fabrication of a PNIPAM-β-CD smart polymer that simultaneously possess chiral recognition and thermosensitive properties. Most importantly, the thermo-induced VPT of the PNIPAM components in response to temperature variations can remarkably affect the inclusion constants of β-CD and the loaded guest molecules in the PNIPAM-β-CD system.[34,35] Inspired by which, we have recently developed a series of smart CMNSs *via* surface decoration of Fe_3O_4 NPs,[36,37] Fe_3O_4 NPs-loaded graphene oxide nanosheets (MGO)[38] and carbon nanotubes (MCNTs)[39] with PNG-β-CD smart polymer chains. The PNG-β-CD smart polymer chains are composed of poly(*N*-isopropylacrylamide-*co*-glycidylmethacrylate) (PNG) copolymer chains with appended rich β-CD hosts, which play a crucial role in effective chiral identification and resolution of various amino acids (AAs) enantiomers. The β-CD units serve as functional receptors or chiral selectors that can specifically recognize and bind L-enantiomer into their cavities to form β-CD/L-enantiomer inclusion complexes. The PNIPAM moieties in the PNG chains act as micro-environmental adjustors for regulating the inclusion constants of β-CD/L-enantiomer. Therefore, those nanoselectors exhibit high chiral recognition and enantioselectivity toward various AAs enantiomers. Most importantly, the desorption of the loaded L-enantiomers and the regeneration of the nanoselectors can be conveniently achieved *via* simply changing the operating temperature.

Molybdenum disulfide (MoS_2) nanosheet, a two-dimensional (2D) transition-metal dichalcogenide material, has attracted widespread interest for the past two decades due to its unique properties, such as large specific surface area, lamellar structure, low manufacturing cost, and simple fabrication.[40–45] This enables it to have significant potentials in a variety of fields including energy storage and conversion,[40,45] sensors,[40,42] optoelectronic devices,[40,43] and drug carriers.[44] Especially, the large specific surface area makes it be an ideal substrate for binding PNG-β-CD chains. Besides, *via* depositing certain amount of Fe_3O_4 NPs on the PNG-β-CD-decorated MoS_2 nanosheets to achieve multifunctional nanocomposite will possess not only high enantioselectivity, but also excellent thermosensitivity and magnetism.

We herein report a PNG-β-CD-modified magnetic MoS_2 nanocomposite ($MMoS_2$/PNG-CD) and explored its potential as a chiral nanoselector for direct enantioseparation of *RS*-PPL. The $MMoS_2$/PNG-CD was prepared *via* a multistep reaction process including solvothermal reaction, surface-initiated atom transfer radical polymerization (SI-ATRP) and a ring-opening reaction. The fabricated $MMoS_2$/PNG-CD simultaneously possesses chiral identification and enantioselectivity toward *RS*-PPL based on the molecular recognition of β-CD and the thermosensitivity of the PNIPAM moieties. Effects of the operating temperature, the initial *RS*-PPL concentration and the molar ratio of glycidylmethacrylate (GMA) to NIPAM on the separation efficiencies of *RS*-PPL were systematically investigated. The results indicate that the operating temperature and the *RS*-PPL concentration strongly affect the resolution efficiencies of *RS*-PPL. Moreover, those parameters were rationally optimized to achieve the optimal separation efficiency of *RS*-PPL. Besides, the desorption of the loaded *R*-PPL molecules and the renewability of the $MMoS_2$/PNG-CD were easily realized *via* simply changing the operating temperature. Such a multifunctional MoS_2 nanocomposite developed herein that possesses a high chiral recognition and enantioselectivity, excellent thermosensitivity and regenerability, is promising to serve as a high-performance nanoselector for direct enantioseparation of various β-blocker drugs.

2. Experimental

2.1. Materials

Sodium molybdate dihydrate ($Na_2MO_4 \cdot 2H_2O$, 99%) and thioacetamide (C_2H_5NS, 98%) were purchased from Aladdin Chemicals (Shanghai, China). Poly(acrylic acid) (PAA, M_w = 1800) was obtained from Sigma-Aldrich Chemicals (Shanghai, China). Iron(iii) chloride hexahydrate ($FeCl_3 \cdot 6H_2O$, 99%), sodium acetate anhydrous (CH_3COONa, 99%), dopamine hydrochloride (DA, 98%) and *RS*-PPL (99%) were bought from Alfa chemicals (Shanghai, China). Tris(hydroxymethyl)aminoethane (Tris, 99.5%), 2-bromoisobutyrylbromide (BiBB, 98%), 2,2′-bipyridine (bpy, 99%), GMA (96%) and NIPAM (98%) were obtained from Tokyo Chemicals Industry (TCI, Japan). NIPAM was purified by recrystallization with a mixture of hexane/acetone (50/50, v/v) before use. Cuprous bromide (CuBr, 99%) and β-CD (99%) were purchased from Kelong Chemicals (Chengdu, China). Ethylenediamine-modified β-CD (EDA-β-CD) was synthesized according to the ref. 46 and 47 Deionized water (18.2 MΩ, 25 °C) from a Milli-Q plus purification system (Millipore) was used throughout the experiments. All other chemicals were analytical grade and used as received.

2.2. Synthesis of MoS_2 nanosheets

MoS_2 nanosheets were synthesized *via* a simple hydrothermal reaction.[45] Briefly, 0.3 g of $Na_2MO_4 \cdot 2H_2O$ and 0.6 g of C_2H_5NS

were dissolved in 40 mL water by ultrasonication for 30 min. Then the obtained solution was transferred in a Teflon-lined stainless-steel autoclave (100 mL) and reacted at 220 °C for 24 h. After natural cooling, the black precipitate was separated by centrifugation (8500 rpm, 15 min) and washed several times with water, and finally dispersed in 50 mL water for the subsequent use.

2.3. Synthesis of $MMoS_2$

The Fe_3O_4 NPs-loaded MoS_2 nanosheets ($MMoS_2$) were synthesized according to the ref. 45 with some modification (Fig. 1a and b). In brief, 15 mL of MoS_2 dispersion (100 mg MoS_2) was mixed with 30 mL of water/ethanol (v/v = 1 : 2) for 1 h under ultrasonication. Then, 0.5 g of $FeCl_3 \cdot 6H_2O$, 0.75 g of CH_3COONa and 100 mg of PAA were added under mechanical stirring for 30 min. After that, the mixture was transferred in a Teflon-lined stainless-steel autoclave (100 mL) and allowed to react at 200 °C for 10 h. After natural cooling, the black precipitate was separated with a permanent magnet and washed several times with water, and then dispersed in 20 mL water for the subsequent use.

2.4. Synthesis of $MMoS_2$/PDA-Br

The magnetic MoS_2 macroinitiator ($MMoS_2$/PDA-Br) was synthesized *via* a two-step reaction process (Fig. 1b–d). First, the PDA-coated $MMoS_2$ ($MMoS_2$/PDA) was prepared according to our recent work.[37–39] In detail, 100 mg of $MMoS_2$ was dispersed in 100 mL Tris–HCl buffer solution (pH = 8.6) in a three-necked flask (150 mL). The Tris–HCl buffer solution was prepared by dissolving 0.26 g of Tris in a mixture solution of ethanol/water (30/70, v/v, 100 mL). Then, 10 mL of DMF dissolved 0.2 g of DA was added dropwise under ultrasonication and allowed the reaction to continue under stirring at 25 °C for 6 h. The black product of $MMoS_2$/PDA was collected with the permanent magnet and washed several times with water, and then dispersed in 30 mL water for subsequent use. The PDA layer provides the $MMoS_2$ with rich catechol and imine functional groups. This offers an ideal platform for immobilizing rich Br atom on the $MMoS_2$ *via* a nucleophilic substitution reaction between the acyl bromide group in BiBB and the –NH_2 and –OH groups on the PDA layer. In detail, 100 mg of $MMoS_2$/PDA was mixed with 20 mL of DMF in a three-necked flask and stirred at 450 rpm for 10 min under N_2 atmosphere and ice bath. Then, 1 mL of triethylamine was added and continued to stir for another 10 min. After that, 20 mL DMF solution contained 0.8 mL BiBB was added dropwise. After reaction for 12 h, the obtained $MMoS_2$/PDA-Br product was collected by a magnet and washed with water several times, and then dispersed in 30 mL water for the further use.

2.5. Synthesis of $MMoS_2$/PNG

The PNG chains-grafted $MMoS_2$ ($MMoS_2$/PNG) was synthesized *via* a SI-ATRP using NIPAM and GMA as the monomers, $MMoS_2$/PDA-Br as the macroinitiator (Fig. 1d and e). Detailly, 100 mg of $MMoS_2$/PDA-Br and various GMA and NIPAM dosages, which represent the molar ratios of 1 : 1 (V_{GMA} = 0.85 mL, m_{NIPAM} = 0.6827 g), 2 : 1 (V_{GMA} = 1.70 mL, m_{NIPAM} = 0.6827 g), 3 : 1 (V_{GMA} = 2.565 mL, m_{NIPAM} = 0.6827 g), and 4 : 1 (V_{GMA} = 3.39 mL, m_{NIPAM} = 0.6827 g), denoted as the $MMoS_2$/PNG1, $MMoS_2$/PNG2, $MMoS_2$/PNG3, and $MMoS_2$/PNG4 samples, respectively, were added in the mixture of methanol/water (15/5, v/v, 20 mL) in a dry Schlenk flask (50 mL) under N_2 atmosphere and magnetic stirring for 20 min. Next, CuBr (0.04 g) and bpy (0.12 g) were added and the mixture was stirred for another 30 min. After three freeze–pump–thaw cycles deoxygenation, the reaction was allowed to last at 55 °C for 6 h. The $MMoS_2$/PNG serial products were obtained and washed with water several times, and then dried in vacuum at 30 °C for 24 h for the subsequent use.

2.6. Synthesis of $MMoS_2$/PNG-CD

The β-CD-modified $MMoS_2$/PNG ($MMoS_2$/PNG-CD) was synthesized as follows (Fig. 1e and f). $MMoS_2$/PNG (0.08 g) and EDA-β-CD (0.75 g) were firstly dispersed in dry DMF (15 mL) under ultrasonication for 30 min. Then the reaction was proceeded at 60 °C for 36 h, and the black $MMoS_2$/PNG-CD product was collected with a magnet and washed with DMF and water several times, and lyophilized. The $MMoS_2$/PNG-CD serial products synthesized using the $MMoS_2$/PNG1, $MMoS_2$/PNG2, $MMoS_2$/PNG3, and $MMoS_2$/PNG4 were denoted as the $MMoS_2$/

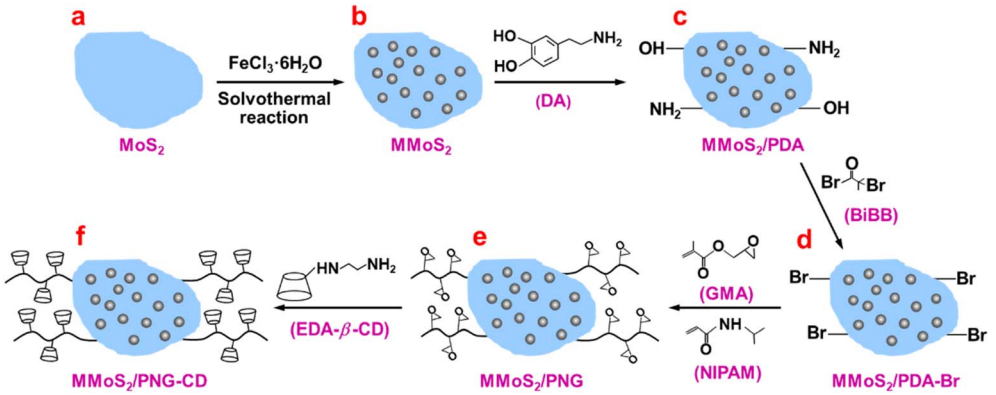

Fig. 1 Schematic illustration of the synthesis process of $MMoS_2$/PNG-CD.

PNG1-CD, $MMoS_2$/PNG2-CD, $MMoS_2$/PNG3-CD, and $MMoS_2$/PNG4-CD, respectively.

2.7. Direct resolution of *RS*-PPL

Direct resolution of *RS*-PPL using $MMoS_2$/PNG-CD was performed as follows. $MMoS_2$/PNG-CD (50 mg) was added in 15 mL *RS*-PPL solution ($C_0 = 0.5$ mM). Then the dispersion was stirred at 25 and 55 °C (below and above the LCST of PNG-β-CD). Next, the enantiomers-loaded $MMoS_2$/PNG-CD was enriched on the wall of vials with a magnet at the predetermined time intervals, and a 150 μL supernatant solution was taken out and filtrated with a microporous membrane (0.22 μm) for the subsequent HPLC measurement. Quantitative analysis of the separation of *RS*-PPL by the $MMoS_2$/PNG-CD was conducted with a HPLC system (Agilent 1200, USA) equipped with a variable wavelength detector (DAD, Agilent Technologies), and the obtained data were analyzed with a HPLC-1200 ChemStation software. Sample tests were carried out with a symmetry shield RP18 column (3.9 × 150 mm, 5 μm, Waters, USA) at 25 °C under a 225 nm UV detector wavelength and 20 μL injection volume (v = 0.8 mL min^{-1}) for the mobile phase. The mobile phase was a mixture of ethanol/ammonium acetate (5/95, v/v, pH 4.5). All the separation experiments were conducted at least twice to guarantee the data accuracy.

To verify the thermosensitive resolution of *RS*-PPL was due to the formation of β-CD/*R*-PPL complexes and the incorporation of PNIPAM moieties, the control trials were performed by the β-CD-free $MMoS_2$/PNG and the PNIPAM-free $MMoS_2$/PG-CD with the same procedure as mentioned above. The separation of *RS*-PPL was evaluated with an enantiomeric excess (ee%) from the peak areas of two isomers in permeates and calculated based on the equation:

$$ee\% = (S_S - S_R)/(S_S + S_R) \times 100\% \quad (1)$$

where S_S and S_R represent the corresponding peak areas of *S*- and *R*-PPL in the filtrate measured by HPLC, respectively.

Besides, since β-CD were tethered in the PNG chains *via* an epoxy ring-opening reaction of the $-NH_2$ group in EDA-β-CD and the epoxy groups in PGMA moieties. The dosage of GMA monomer will certainly affect the binding amount of β-CD significantly, thus the separation efficiencies of *RS*-PPL. Therefore, effect of the molar ratios of GMA to NIPAM ($n_{GMA} : n_{NIPAM}$ = 1 : 1, 2 : 1, 3 : 1 and 4 : 1) on the separation efficiencies of the resulted $MMoS_2$/PNG*i*-CD products (i = 1, 2, 3, and 4) were also studied. Besides, to investigate the effect of the initial *RS*-PPL concentration on the resolution performance of the $MMoS_2$/PNG-CD, the *RS*-PPL concentration varied from 0.1 to 1 mM while sustaining the other conditions invariable during the separation experiments. To explore the reusability of the nanoselector, the used $MMoS_2$/PNG-CD was washed with hot/cold water in turn by ultrasonication for the next cycle.

2.8. Characterization

Transmission electron microscope (TEM) images were obtained with a JEM-2010 microscope (JEOL, Japan) at an accelerating voltage of 120 kV. The samples were prepared by drop-casting a dilute solution of particles onto carbon-coated copper grids, followed by air drying. High-resolution transmission electron microscopy (HRTEM) images were obtained on a field-emission electron microscope (FEI Talos F200x, USA) equipped with a Super X energy spectrum. X-ray photoelectron spectroscopy (XPS) measurements were performed on a Thermo Fischer ESCALAB 250Xi (USA). Structural information of the samples was obtained by X-ray diffractometer-6100 diffractometer (Shimadzu, Japan). Fourier transform infrared spectrometry (FT-IR) analysis was conducted on an IR 200 spectrometer (Thermo Nicolet, USA) using KBr pellets. Thermogravimetric analysis (TGA) was performed on a Mettler TGA/SDTA851e° instrument (Switzerland) at a heating rate of 5 °C min^{-1} from 30 to 700 °C under N_2 atmosphere. The magnetism of the samples was measured with a vibrating sample magnetometer (VSM) on a model 2000 physical property measurement system (Quantum design) at room temperature.

3. Results and discussion

3.1. Fabrication and characterization of materials

The synthesis process of the material is schematically illustrated in Fig. 1. MoS_2 nanosheets with a large specific surface area were used as the substrate for binding PNG-β-CD smart polymer chains. Fe_3O_4 NPs were firstly deposited on the MoS_2 nanosheets to endow them with magnetic separability (Fig. 1a and b) then the PDA functional layer is coated on the $MMoS_2$ to offer the nanosheets rich active sites ($-NH_2$ and –OH groups) (Fig. 1b and c), and plentiful of Br atoms were introduced on the $MMoS_2$ *via* a nucleophilic substitution reaction between the acyl bromide group in BiBB molecule and the $-NH_2$ and –OH groups on the PDA layer (Fig. 1c and d). The PNIPAM moieties were introduced in the PNG-β-CD to facilitate the $MMoS_2$ with thermosensitive resolution ability and convenient regenerability *via* simply changing the operating temperature. Rich β-CD hosts were bound to the PNG *via* an epoxy ring-opening reaction of epoxy groups in PGMA and the $-NH_2$ group in EDA-β-CD to endow the $MMoS_2$ nanocomposite with high enantioselectivity toward various chiral compounds (Fig. 1e and f).

Effect of the amount of Fe_3O_4 NPs deposited on the MoS_2 on the separation performances of the MoS_2 functional nanocomposite was also investigated by the different samples synthesized with various $FeCl_3 \cdot 6H_2O$ dosages (0.2, 0.5, and 1.0 g), since the Fe^{3+} concentration in the feed reactants strongly affects the loading amount of Fe_3O_4 NPs. As observed in Fig. S1a,† the samples synthesized with a smaller (0.2 g) or a larger dosage of $FeCl_3 \cdot 6H_2O$ (1.0 g) (denoted the $MMoS_2$-0.2 and $MMoS_2$-1.0, respectively) show undesirable magnetism. The $MMoS_2$-0.2 exhibits a poor magnetic separability owing to that a low Fe^{3+} concentration in the reactant leads to a small loading amount of Fe_3O_4 NPs. Therefore, it was difficult to be collected by a magnet even after 24 h. For a larger dosage (1.0 g), the prepared $MMoS_2$-1.0 exhibits poor water dispersibility (Fig. S1b†). Rapid enrichment of the sample particles on the vial wall is observed. The undesirable aggregations of the $MMoS_2$-1.0 will dramatically reduce the specific surface area of the

$MMoS_2$ substrate, and thus the grafting density of PNG-β-CD as well as the binding amount of β-CD, and finally the separation efficiencies of *RS*-PPL. Therefore, the $MMoS_2$-0.5 sample with a relatively high specific surface area and a satisfactory magnetism was chosen as the substrate for the subsequent grafting reactions. Besides, at a small $FeCl_3 \cdot 6H_2O$ dosage, the typical Fe–O peak at 584 cm^{-1} from the Fe_3O_4 NPs on the MoS_2 is observable and the peak intensity is quite weak (Fig. S2†). While with increasing the dosage to 1.0 g, the Fe–O peak shifts from 584 to 536 cm^{-1} and becomes much stronger. This indicates that a larger $FeCl_3 \cdot 6H_2O$ dosage causes a larger loading amount of Fe_3O_4 NPs on the MoS_2. Higher loading amount will inevitably decrease the specific surface area of the $MMoS_2$ substrate, and thus the grafting density of PNG-β-CD as well as the binding amount of β-CD, and finally the resolution efficiencies of *RS*-PPL. Therefore, the $MMoS_2$-0.5 sample with a compromising performance of specific surface area and magnetic property (abbreviated $MMoS_2$) was employed for the following grafting of PNG-CD functional polymer chains.

The morphology and microstructures of the functional $MMoS_2$ nanocomposites were observed by TEM. As shown in Fig. 2a, the primitive MoS_2 nanosheets character a 2D fold laminar structure. After solvothermal reaction, Fe_3O_4 NPs with sizes of 20–50 nm are clearly observed on the MoS_2 (Fig. 2b), which endow the nanosheets with convenient magnetic separability from enantiomeric solutions under an external magnetic field (EMF). The HRTEM image shows that the loaded Fe_3O_4 NPs have a spherical structure and good dispersibility (Fig. S3a†). Further magnifying one of the particles, a clear and obvious lattice fringes is observed (Fig. S3b†). Measuring the distance between two adjacent planes in a specific direction gives a value of 0.48 nm, corresponding to the lattice spacing of (111) planes of cubic magnetite. The cubic crystal lattice is determined by SAED, as shown in Fig. S3c.† The XRD pattern shows that the peaks at 18.3, 30.0, 35.5, 43.1, 53.4, 57.0, and 62.6° are marked by the indices (111), (220), (311), (400), (422), (511), and (440) of Fe_3O_4 phases (Fig. S3d†). These peaks coincide with those of standard patterns (JCPDS no. 19-0629), confirming the formation of the cubic phase. Besides, XPS analysis provides detailed information on the chemical compositions of the $MMoS_2$. As shown in Fig. S4,† the binding energy of Fe $2p_{3/2}$ and Fe $2p_{1/2}$ for Fe_3O_4 is around 711.1 and 724.5 eV, respectively, which further confirm the particles are Fe_3O_4 NPs.[48] After coating with a PDA layer on the surface, a thin organic matter of PDA is clearly observed on the $MMoS_2$ (Fig. 2c). After further modification with BiBB, the $MMoS_2$/PDA-Br does not show a noticeable change in the surface microstructures due to the introduction of monolayer BiBB (Fig. 2d). When the PNG2 chains are grafted onto the $MMoS_2$ *via* a SI-ATRP reaction, black organic substance corresponding to the PNG2 chains are witnessed on the nanosheets (Fig. 2e). After the subsequent binding of β-CD in the PNG2, the morphology of the $MMoS_2$/PNG2-CD changes little, and only slight agglomeration of the sample is observed, indicating that the incorporation of β-CD has little effect on the morphology and microstructure of the sample (Fig. 2f). Those results indicate the successful synthesis of the $MMoS_2$/PNG2-CD.

The successful fabrication of the $MMoS_2$/PNG-CD is also verified by the FT-IR results. As displayed in Fig. 3a, for the $MMoS_2$, two characteristic peaks at 572 and 1716 cm^{-1} correspond to the stretching vibration of Fe–O and C=O stretching vibration of PAA stabilizers, respectively.[49] For the $MMoS_2$/PDA,

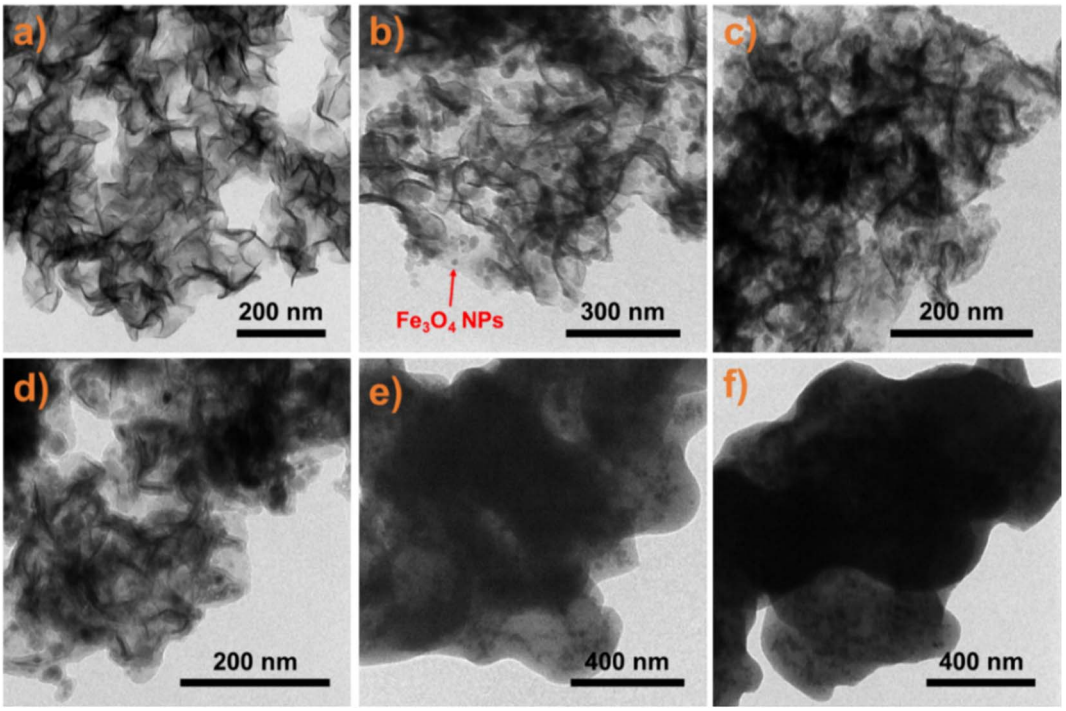

Fig. 2 Typical TEM images of (a) MoS_2, (b) $MMoS_2$, (c) $MMoS_2$/PDA, (d) $MMoS_2$/PDA-Br, (e) $MMoS_2$/PNG2, and (f) $MMoS_2$/PNG2-CD.

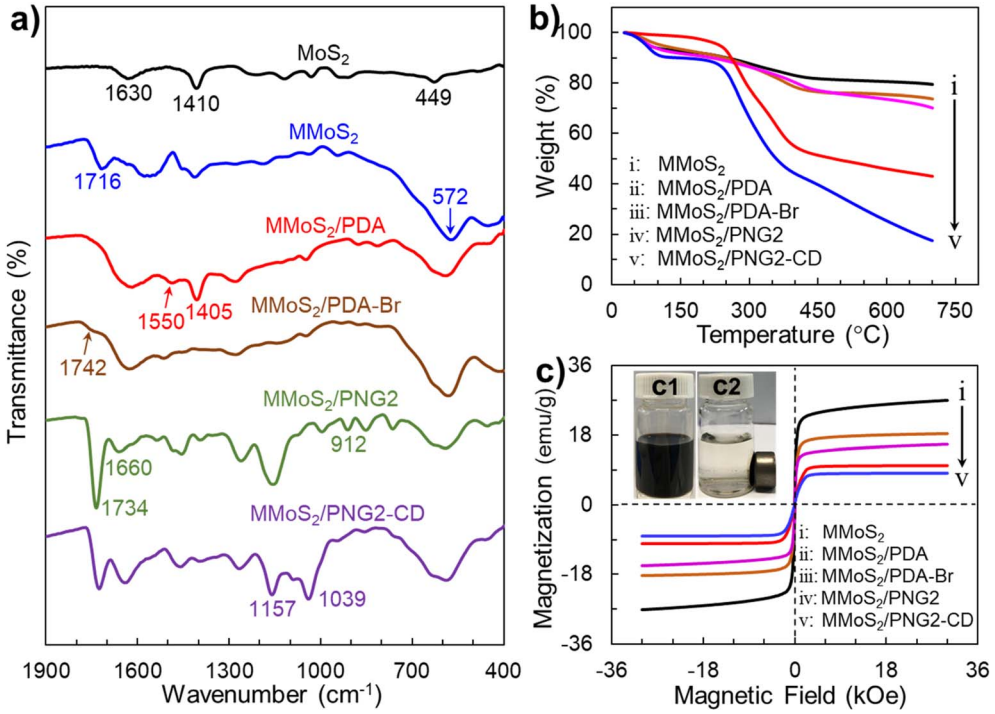

Fig. 3 FT-IR spectra (a), TGA curves (b), and hysteresis loops (c) of MoS_2, $MMoS_2$, $MMoS_2$/PDA, $MMoS_2$/PDA-Br, $MMoS_2$/PNG2 and $MMoS_2$/PNG2-CD. The insets in (c) show the photographs of the $MMoS_2$/PNG2-CD before (c1) and after (c2) magnetic separation.

the typical absorption peaks of 1400–1700 cm^{-1} are ascribed to the stretching vibrations of N–H and benzene rings of PDA, indicating the coating of PDA layer on the $MMoS_2$.[37,39] After anchoring BiBB molecules on the $MMoS_2$/PDA, a weak characteristic peak of C=O stretching vibration at 1742 cm^{-1} in BiBB is observed from the spectrum of the $MMoS_2$/PDA-Br.[37,39] When the SI-ATRP reaction between GMA and NIPAM with a molar ratio of 2 : 1 occurs on the $MMoS_2$/PDA-Br, the absorption peaks at 912 and 1734 cm^{-1} owing to the C–O–C and C=O stretching vibrations in PGMA are all observed.[37,39] Besides, the typical peak at 1660 cm^{-1} due to the stretching vibration of C=O in PNIPAM moieties is also observed for the spectrum of the $MMoS_2$/PNG. This indicates the successful grafting of PNG on the $MMoS_2$/PDA.[37,39] For the $MMoS_2$/PNG2-CD, the characteristic peaks at 1039 and 1157 cm^{-1} come from the antisymmetric vibrations of the C–O–C and the C–C/C–O of β-CD, respectively. Moreover, the typical peak of the epoxy groups in PGMA at 912 cm^{-1} disappears.[37,39] This indicates the successful synthesis of the $MMoS_2$/PNG2-CD again.

Besides, the TGA results also confirm the successful fabrication of the $MMoS_2$/PNG-CD. Fig. 3b shows the TG results of the MoS_2, $MMoS_2$, $MMoS_2$/PDA, $MMoS_2$/PDA-Br, $MMoS_2$/PNG2, and $MMoS_2$/PNG2-CD. The gradual increase in weight loss of each sample is mainly arisen from the decomposition of organic substances introduced on the $MMoS_2$. For the $MMoS_2$, a weight loss of 20.59% from 25 to 700 °C is owing to the evaporation of the physically adsorbed water and the decomposition of PAA stabilizers on the $MMoS_2$. After PDA coating on the $MMoS_2$, the weight loss increases by 5.65% attributed to the decomposition of PDA layer in the same temperature range. For the $MMoS_2$/PDA-Br, an additional weight loss of ~3.6% compared with the $MMoS_2$/PDA is thanks to the decomposition of BiBB attached in the PDA layer. After the grafting of PNG2 copolymer chains on the $MMoS_2$/PDA-Br, the weight loss increases by ~27.16% due to the decomposition of PNG2 chains. The binding amount of PNG2 is 387.2 mg g^{-1} based on the weight loss data. After a ring-opening reaction between the epoxy groups in PGMA and the $-NH_2$ group in EDA-β-CD, rich β-CD hosts are tethered in the PNG2, giving rise to the formation of the $MMoS_2$/PNG2-CD. An additional mass loss of ~25.58% in comparison with that of the $MMoS_2$/PNG2 is owing to the decomposition of β-CD in the PNG2. The binding amount of β-CD is calculated to be 595.0 mg g^{-1}. Those results further confirm the successful fabrication of the $MMoS_2$/PNG2-CD. The large binding of β-CD greatly benefits from incensing the enantioselectivity of the $MMoS_2$/PNG2-CD toward *RS*-PPL.

The elemental analysis results of the MoS_2 nanocomposites also verify the successful preparation of the $MMoS_2$/PNG-CD. As shown in Table 1, the element S in all samples come from MoS_2, and their content gradually reduces from the $MMoS_2$ to the

Table 1 The elemental analysis of the functional MoS_2 serial samples

Sample	N (%)	C (%)	H (%)	S (%)
$MMoS_2$	0.160	1.585	0.557	18.72
$MMoS_2$/PDA	1.930	17.24	1.462	9.116
$MMoS_2$/PDA-Br	2.495	21.61	1.241	6.275
$MMoS_2$/PNG2	3.125	33.18	3.532	5.21
$MMoS_2$/PNG2-CD	3.225	44.61	6.335	0.744

$MMoS_2$/PNG2-CD due to the introduction of PDA layer, BiBB and PNG-β-CD. The element N origins from PDA layer for the $MMoS_2$/PDA, from PNIPAM moieties for the $MMoS_2$/PNG2 and from EDA-β-CD for the $MMoS_2$/PNG2-CD. As seen from Table 1, the content of N, C, and H in the $MMoS_2$/PDA sample increases significantly compared with that of the $MMoS_2$, indicating the coating of PDA layer on the $MMoS_2$. For the $MMoS_2$/PNG2, the content of C and H increases obviously, showing the grafting of PNG2 chains on the $MMoS_2$. The content of C and H increases evidently after a ring-opening reaction between the epoxy groups in PGMA and the $-NH_2$ group in EDA-β-CD. This results imply the successful incorporation of β-CD into the PNG2, thus causing the formation of $MMoS_2$/PNG2-CD.

Depositing certain amount of Fe_3O_4 NPs on the MoS_2 endows them with convenient magnetic separability from the enantiomeric solution under an EMF. VSM technique was used to characterize the magnetism of the MoS_2 functional nanocomposite in this study. As shown in Fig. 3c, the magnetization saturation (M_s) values of the $MMoS_2$, $MMoS_2$/PDA, $MMoS_2$/PDA-Br, $MMoS_2$/PNG2, and $MMoS_2$/PNG2-CD are 27.03, 18.34, 15.74, 10.07 and 8.09 emu g^{-1}, respectively. The gradual reduction in M_s values is mainly due to the introduction of non-magnetic organic substances including PAA stabilizers, PDA layer, BiBB, PNG2-β-CD on the $MMoS_2$. While the as-synthesized $MMoS_2$/PNG2-CD still shows excellent magnetism. Besides, the magnetic hysteresis loop of the sample measured in a small measurement range (−500–500 Oe) passes through the origin, and there are almost no residual magnetization and coercive force are observed (Fig. S5†), indicating that the synthesized $MMoS_2$/PNG2-CD is superparamagnetic. Moreover, the $MMoS_2$/PNG2-CD can be easily separated from the water within 3 min under an EMF (inset c2 in Fig. 3c), and redispersed in the water rapidly *via* slight shaking (inset c1 in Fig. 3c). Such excellent magnetism of the $MMoS_2$/PNG2-CD makes it convenient recovery from the *RS*-PPL solution.

3.2. Direct resolution of *RS*-PPL by $MMoS_2$/PNG-CD

To verify that β-CD in the PNG-β-CD play a crucial role in the chiral identification and resolution of *RS*-PPL, the separation of the β-CD-contained $MMoS_2$/PNG2-CD and the β-CD-free $MMoS_2$/PNG2 toward *RS*-PPL (C_0 = 0.5 mM) was firstly investigated at 25 °C. As observed from Fig. 4a, the $MMoS_2$/PNG2-CD shows a high enantioselectivity toward *RS*-PPL, and the ee% can reach 19.64% after interaction for 28 h. As mentioned above, β-CD has a hydrophobic cavity, numerous guests can be accommodated in its cavity to form inclusion complexes *via* various interactions such as van der Waals forces, hydrophobic interactions, and hydrogen bonding interactions. Although *S*- and *R*-PPL can form complexes with β-CD since the hydrophobic naphthalene ring of both two enantiomers can permeate into the β-CD cavity, the 3D structures of *S*- and *R*-PPL with respect to the position of –OH group at the chiral center of the two enantiomers are significantly different.[33,50] Compared with the *S*-enantiomer, the intermolecular hydrogen bonds between the –OH group of *R*-PPL and the second hydroxyl groups (–(HO)$_s$) of β-CD rims are formed more favorably,[33] thus giving

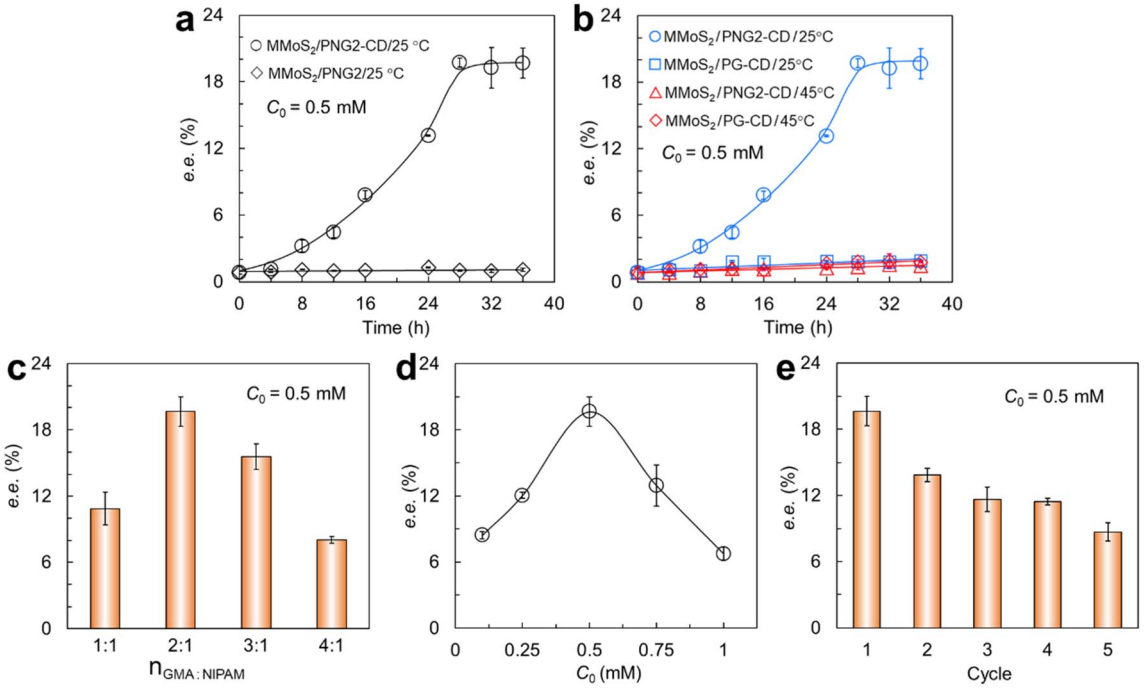

Fig. 4 (a) Separation performances of the β-CD-contained $MMoS_2$/PNG2-CD and the β-CD-free $MMoS_2$/PNG2 toward *RS*-PPL at 25 °C. (b) Separation performances of the PNIPAM-contained $MMoS_2$/PNG2-CD and the PNIPAM-free $MMoS_2$/PG-CD toward *RS*-PPL at 25 and 45 °C. (c) Separation of *RS*-PPL by the $MMoS_2$/PNG-CD serials samples synthesized with the different molar ratios of GMA to NIPAM. (d) Effect of the initial *RS*-PPL concentration on the separation performances of the $MMoS_2$/PNG2-CD. (e) The reusability of the $MMoS_2$/PNG2-CD. The concentration of *RS*-PPL in (a)–(c), and (e) is 0.5 mM.

rise to a higher selectivity of the $MMoS_2$/PNG2-CD toward *R*-PPL over *S*-PPL at 25 °C. For the $MMoS_2$/PNG2, since the absence of β-CD in the PNG2, therefore, it shows never a noticeable enantioselectivity toward *RS*-PPL. As observed in Fig. 4a, the maximal ee value is only 1.27% (diamond). Moreover, the operating temperature significantly affects the separation of *RS*-PPL (Fig. 4b). At the temperature lower than the LCST of the PNG-β-CD (such as 25 °C), the PNIPAM chains in the PNG-β-CD are hydrophilic and swollen. At this case, rich β-CD hosts can specifically recognize and bind *R*-PPL to form stable complexes since the inclusion constants of β-CD/*R*-PPL are large,[37,39] thus yielding a high enantioselectivity of the $MMoS_2$/PNG2-CD. While at 45 °C, higher than the LCST, the ee value increases slowly and just reaches a small value (less than 2%) even prolonging the contact time up to 36 h (triangle, Fig. 4b). This is because that PNIPAM chains in the PNG-β-CD become hydrophobic and shrunken under this circumstance, effect of the steric hindrance from the shrinking and crowded PNIPAM chains results in a significant reduction in the inclusion constants of β-CD/*R*-PPL,[34,35] thus generating a low enantioselectivity of the $MMoS_2$/PNG2-CD. This indicates that β-CD on the $MMoS_2$/PNG2-CD play an important role in the enantioseparation of *RS*-PPL. The thermosensitive chiral recognition and enantioseparation of the $MMoS_2$/PNG2-CD toward *RS*-PPL is ascribed to the incorporation of PNIPAM moieties into the PNG-β-CD.

As mentioned above, β-CD hosts play a pivotal role in the chiral recognition and enantioseparation of *RS*-PPL, which are bound in the PNG *via* a ring-opening reaction between the epoxy groups in PGMA and the $-NH_2$ group in EDA-β-CD. Therefore, upon keeping the usage of NIPAM invariable, the molar ratio of GMA to NIPAM (n_{GMA}/n_{NIPAM}) will significantly affect the binding amount of β-CD in the PNG, and thus the hydrophilicity/hydrophobicity and the enantioselectivity of the $MMoS_2$/PNG-CD. As observed in Fig. 4c, the ee value increases with increasing the n_{GMA}/n_{NIPAM} value from 1 to 2 at first, and then reduces gradually upon further enhancing from 2 to 4. The number of the epoxy groups in PNG increases with increasing the n_{GMA}/n_{NIPAM} value, thus a higher binding amount of β-CD in the PNG-β-CD. A high binding amount of β-CD offers more active sites for interacting with *R*-PPL, thus causing a larger ee value. When the n_{GMA}/n_{NIPAM} value is larger than 2, the hydrophobicity of the $MMoS_2$/PNG3 and $MMoS_2$/PNG4 samples becomes stronger and stronger with increasing the GMA dosage. As a result, the reactive sites (epoxy groups) available in the PNG are relatively inadequate since the shrinkage of the PNG. Consequently, the PNG-β-CD chains become more hydrophobic, which worsens the dispensability of the $MMoS_2$/PNG3-CD and $MMoS_2$/PNG4-CD in water (Fig. S6†). In this case, only small amount of β-CD on the $MMoS_2$/PNG-CD can interact with *R*-PPL, thus leading to small ee values. As observed from Fig. 4c, the optimal n_{GMA}/n_{NIPAM} value for the synthesis of the

Table 2 Comparison of the resolution performances of the $MMoS_2$/PNG-CD and other conventional methods[a]

Chiral selectors	Analyte	Interaction	Operation	Cost	Separation efficiency	Separation mode	Recyclability	Ref.
Chiral 3D HOIZA	2-Butanol and methyl-1-butano	Inclusion complexation	Complex	Low	ee = 8.4–98.2%	Direct	Yes	51
Ovomucoid chiral column	Carvedilol, pindolol and oxprenolol	Hydrogen bonds	Complex	High	R_s = 1.75–2.15	Indirect	No	9
Chiral-mesoporous-polypyrrole NPs	Valine	Not mentioned	Complex	High	ee = 54%	Indirect	No	52
β-CD-modified AuNPs	DL-Val, Leu, Glu, Asp; chlorpheniramine, zopiclone and carvedilol	Inclusion complexation	Complex	High	α = 1.02–1.045	Indirect	No	53
β-CD-modified MWNTs, PS, TiO_2, and Al_2O_3	Clenbuterol	Inclusion complexation	Complex	High	α = 1.023–1.034	Indirect	No	54
Au(110) surface	Valine	S–Au, N–Au, and hydrogen bonds	Complex	High	Not mentioned	Indirect	No	55
CM-β-CD	Carteolol, atenolol, sotalol, metoprolol, esmolol and propranolol	Inclusion complexation and hydrogen bonds	Complex	High	R_s = 1.0–3.0	Indirect	No	15
CM-β-CD, β-CD, and HP-β-CD	Betaxolol, sotalol, metoprolol, bisoprolol, bevantolol, and timolol	Not mentioned	Complex	High	R_s = 0.98–2.50	Indirect	No	16
Ionic liquid cooperate with DM-β-CD and TM-β-CD	Pindolol, oxprenolol and propranolol	Hydrogen bonds, hydrophobic interactions and ion-dipole	Complex	High	α = 0.45–1.39	Indirect	No	17
$MMoS_2$/PNG-CD	Propranolol	Inclusion complexation	Simple	Low	ee = 19.64%	Direct	Yes	This work

[a] PS, polystyrene; MWNTs, multi-walled nanotubes; CM-β-CD, carboxymethyl-β-cyclodextrin; HP-β-CD, hydroxypropyl-β-cyclodextrin; DM-β-CD, 2,6-di-*O*-methyl-β-cyclodextrin; TM-β-CD, 2,3,6-tri-*O*-methyl-β-cyclodextrin; ee, enantiomeric excess; R_s, separation resolution; and α, separation factor.

$MMoS_2$/PNG-CD with high enantioselectivity is 2. Therefore, the fabricated $MMoS_2$/PNG2-CD was chosen to perform the material characterizations and the subsequent separation experiments. Incorporation of PNIPAM moieties into the PNG-β-CD endows the $MMoS_2$/PNG2-CD with excellent thermosensitivity (Fig. S7†), thus making the loaded *R*-PPL molecules release from the MoS_2 functional nanocomposite and the facile regeneration of the material. Therefore, the resolution of *RS*-PPL should be operated at temperatures below the LCST of the PNG2-β-CD (25 °C) (circle, Fig. 4b), and the regeneration of the material can be operated at the temperature higher than the LCST (such as 45 °C) (triangle, Fig. 4b).

The initial concentration of chiral compounds is another factor that significantly affects the separation performances of a nanoselector. Therefore, the effect of the initial *RS*-PPL concentration on the resolution performances of the $MMoS_2$/PNG2-CD was also investigated in this work. As observed in Fig. 4d, the ee value increases with increasing the *RS*-PPL concentration from 0 to 0.5 mM, and then gradually decrease at the concentration is over 0.5 mM. At low *RS*-PPL concentrations (lower than 0.5 mM), the number of β-CD is relatively excessive compared with that of *R*-PPL molecules. β-CD can bind more *R*-PPL to form β-CD/*R*-PPL complexes, thus yielding larger ee values. While upon further increasing the *RS*-PPL concentration, the number of β-CD become relatively insufficient than that of *R*-PPL, thus resulting in lower ee values. However, the $MMoS_2$/PNG2-CD still show certain separation ability toward *RS*-PPL, and the optimal resolution concentration of *RS*-PPL is 0.5 mM.

On account of excellent magnetic and thermosensitive properties of the $MMoS_2$/PNG-CD, it can easily recycled with an EMF and *via* simply changing the operating temperature. For this purpose, the *R*-PPL-loaded $MMoS_2$/PNG2-CD was washed with hot/cool water (45 and 25 °C) alternatively under ultrasonication, and the adsorbed *R*-PPL molecules could be readily eluted from the material. As displayed in Fig. 4d, the used $MMoS_2$/PNG2-CD shows good regenerability after consecutive five cycles. Although the ee value reduces slightly with an increase in the cycles, it can still reach 8.69%. The slight reduction in ee values is presumably arisen from that some parts of *R*-PPL molecules on the material were not desorbed. Moreover, certain amount of material suffered from weight loss during the washing process. Our developed $MMoS_2$/PNG-CD when used for enantiomeric separations possesses some obvious advantages compared to those conventional methods (Table 2), such as simplicity in operation, inexpensiveness, relatively higher selectivity, and easy recyclability of the material, which indicates that the $MMoS_2$/PNG2-CD is promising to serve as an excellent nanoselector for direct enantiomeric resolution of various β-blocker drugs.

4. Conclusions

In summary, a novel chiral magnetic molybdenum disulfide nanocomposite ($MMoS_2$/PNG-CD) with a high enantioselectivity and excellent thermosensitivity and magnetism has been fabricated *via* a multistep reaction process. The resolution of the prepared $MMoS_2$/PNG-CD toward a chiral drug *RS*-PPL is systematically investigated. The obtained results indicate that β-CD on the $MMoS_2$/PNG-CD play a crucial role in the chiral discrimination and enantioseparation of *RS*-PPL. The thermosensitive chiral recognition and resolution of *RS*-PPL by the $MMoS_2$/PNG-CD is due to the incorporation of PNIPAM moieties into the PNG-β-CD chains. The molar ratio of GMA to NIPAM (n_{GMA} : n_{NIPAM}) and the initial *RS*-PPL concentrations are two important factors that significantly affect the separation efficiencies of *RS*-PPL, the optional n_{GMA} : n_{NIPAM} value and the *RS*-PPL initial concentration are respectively 2 and 0.5 mM to achieve a satisfactory resolution efficiency. Besides, the used $MMoS_2$/PNG-CD can be easily recovered under an external magnetic field and regenerated *via* simply changing the operating temperature. Such a multifunctional MoS_2 nanocomposite developed herein with a high enantioselectivity, excellent thermosensitivity and regenerability can serve as a high-performance nanoselector for direct enantioseparation of various β-blocker drugs.

Author contributions

H. R. Yu and L. Lei: conceptualization, validation, investigation, software, data curation, formal analysis, writing – original draft; Y. L. Wang and X. Wang: investigation and data curation for the revised manuscript. T. Liang: methodology, investigation, funding acquisition, writing – review and editing, supervision; C. J. Cheng: conceptualization, funding acquisition, writing – review and editing.

Conflicts of interest

The authors declare that they have no competing interests.

Acknowledgements

This work was financially supported by the National Natural Science Foundation of China (21676219), the Sichuan Science and Technology Program (2022NSFSC1198) and the Fundamental Research Funds for Central Universities, Southwest Minzu University (2020NYBPY12).

References

1 J. J. D. De Jong, L. N. Lucas, R. M. Kellogg, J. H. van Esch and B. L. Feringa, *Science*, 2004, **304**, 278–281.
2 S. Che, Z. Liu, T. Ohsuna, K. Sakamoto, O. Terasaki and T. Tatsumi, *Nature*, 2004, **429**, 281–284.
3 G. K. E. Scriba, *Chromatographia*, 2012, **75**, 815–838.
4 I. Agranat and H. Caner, *Drug Discovery Today*, 1999, **4**, 313–321.
5 N. M. Maier, P. Franco and W. Lindner, *J. Chromatogr. A*, 2001, **906**, 3–33.
6 N. Y. Rahim, K. S. Tay and S. Mohamad, *J. Inclusion Phenom. Macrocyclic Chem.*, 2016, **85**, 303–315.
7 J. Wu, X. Xiao, Z. Li and L. Jia, *Anal. Bioanal. Chem.*, 2019, **411**, 2121–2129.

8 S. Alwera and R. Bhushan, *Biomed. Chromatogr.*, 2016, **30**, 1772–1781.
9 S. Imre, A. Ormenişan, A. Tero-Vescan, D. L. Muntean and C. E. Vari, *J. Chromatogr. Sci.*, 2016, **54**, 1578–1583.
10 I. Ali, V. D. Gaitonde, H. Y. Aboul-Enein and A. Hussain, *Talanta*, 2009, **78**, 458–463.
11 M. J. Paik, D. T. Nguyen and K. R. Kim, *J. Chromatogr. A*, 2006, **1103**, 177–181.
12 M. D. Bubba, L. Checchini and L. Lepri, *Anal. Bioanal. Chem.*, 2013, **405**, 533–554.
13 J. Zheng, D. Norton and S. A. Shamsi, *Anal. Chem.*, 2006, **78**, 1323–1330.
14 J. Zheng and S. A. Shamsi, *Electrophoresis*, 2006, **27**, 2139–2151.
15 L. Huang, J. M. Lin, L. S. Yu, L. Xu and G. Chen, *Electrophoresis*, 2008, **29**, 3588–3594.
16 H. Zhang, H. Shao, Y. A and Z. Zhang, *Chromatographia*, 2008, **68**, 653–658.
17 Y. Jin, C. Chen, L. Meng, J. Chen, M. Li and Z. Zhu, *Talanta*, 2012, **89**, 149–154.
18 J. Wu, P. Su, J. Huang, S. Wang and Y. Yang, *J. Colloid Interface Sci.*, 2013, **399**, 107–114.
19 Y. Wang, P. Su, S. Wang, J. Wu, J. Huang and Y. Yang, *J. Mater. Chem. B*, 2013, **1**, 5028–5035.
20 J. Wu, P. Su, Y. Yang, J. Huang, Y. Wang and Y. Yang, *J. Mater. Chem. B*, 2014, **2**, 775–782.
21 J. Huang, P. Su, J. Wu and Y. Yang, *RSC Adv.*, 2014, **4**, 58514–58521.
22 J. Wu, P. Su, D. Guo, J. Huang and Y. Yang, *New J. Chem.*, 2014, **38**, 3630–3636.
23 A. Sikora, D. Chełminiak-Dudkiewicz, M. Ziegler-Borowska and M. P. Marszałł, *Tetrahedron: Asymmetry*, 2017, **28**, 374–380.
24 A. P. Kumar, J. H. Kim, T. D. Thanh and Y. Lee, *J. Mater. Chem. B*, 2013, **1**, 4909–4915.
25 R. P. Liang, X. Y. Meng, C. M. Liu, J. W. Wang and J. D. Qiu, *Microfluid. Nanofluid.*, 2014, **16**, 195–206.
26 X. Ma, W. Du, Y. Li, C. Hua, A. Yu, W. Zhao, S. Zhang and F. Xie, *J. Pharm. Biomed. Anal.*, 2019, **172**, 50–57.
27 A. T. M. Da Silva, B. C. Pires, L. A. F. Dinali, A. C. F. C. Maia, C. J. Santos, C. Sanches, W. S. Borges and K. B. Borges, *Sep. Purif. Technol.*, 2021, **261**, 118257–118267.
28 S. Ghosh, Q. J. Teck, M. Uddin and K. Hidajat, *Chin. J. Chem. Eng.*, 2014, **28**, 14–21.
29 Y. Wang and A. M. Chen, *Org. Process Res. Dev.*, 2008, **12**, 282–290.
30 Y. Wei, A. Tian, Y. Li, X. Wang and B. Cao, *J. Mater. Chem.*, 2012, **22**, 8499–8504.
31 H. Su, Q. Zheng and H. Li, *J. Mater. Chem.*, 2012, **22**, 6546–6548.
32 H. G. Schild, *Prog. Polym. Sci.*, 1992, **17**, 163–249.
33 Y. Tao, J. Dai, Y. Kong and Y. Sha, *Anal. Chem.*, 2014, **86**, 2633–2639.
34 T. Nozaki, Y. Maeda, K. Ito and H. Kitano, *Macromolecules*, 1995, **28**, 522–524.
35 H. Ohashi, Y. Hiraoka and T. Yamaguchi, *Macromolecules*, 2006, **39**, 2614–2620.
36 Y. Y. Song, X. D. Song, H. Yuan and C. J. Cheng, *New J. Chem.*, 2016, **40**, 3194–3207.
37 H. Y. Zhu, X. D. Song, X. R. Yang, C. J. Cheng, H. R. Yu and H. H. Zhang, *J. Mater. Sci.*, 2019, **54**, 2960–2974.
38 X. R. Yang, X. D. Song, H. Y. Zhu, C. J. Cheng, H. R. Yu and H. H. Zhang, *ACS Appl. Bio Mater.*, 2018, **1**, 1074–1083.
39 X. R. Yang, L. Lei, Z. Peng, H. R. Yu and C. J. Cheng, *Anal. Methods*, 2019, **11**, 5953–5962.
40 X. Zhang, Z. Lai, C. Tan and H. Zhang, *Angew. Chem., Int. Ed.*, 2016, **55**, 8816–8838.
41 X. Huang, Z. Zeng, S. Bao, M. Wang, X. Qi, Z. Fan and H. Zhang, *Nat. Commun.*, 2013, **4**, 1–8.
42 F. Zhang, C. Lu, M. Wang, X. Yu, W. Wei and Z. Xia, *ACS Sens.*, 2018, **3**, 304–312.
43 Z. Yin, H. Li, H. Li, L. Jiang, Y. Shi, Y. Sun, G. Lu, Q. Zhang, X. Chen and H. Zhang, *ACS Nano*, 2012, **6**, 74–80.
44 T. Liu, C. Wang, X. Gu, H. Gong, L. Cheng, X. Shi, L. Feng, B. Sun and Z. Liu, *Adv. Mater.*, 2014, **26**, 3433–3440.
45 Y. Chen, B. Song, X. Tang, L. Lu and J. Xue, *Small*, 2014, **10**, 1536–1543.
46 R. C. Petter, J. S. Salek, C. T. Sikorski, G. Kumaravel and F. T. Lin, *J. Am. Chem. Soc.*, 1990, **112**, 3860–3868.
47 Y. Y. Liu, X. D. Fan and L. Gao, *Macromol. Biosci.*, 2003, **3**, 715–719.
48 H. T. Cui, Y. Liu and W. Z. Ren, *Adv. Powder Technol.*, 2013, **24**, 93–97.
49 Y. Y. Xu, M. Zhou, H. J. Geng, J. J. Hao, Q. Q. Ou, S. D. Qi, H. L. Chen and X. G. Chen, *Appl. Surf. Sci.*, 2012, **258**, 3897–3902.
50 R. Stiufiuc, C. Iacovita, G. Stiufiuc, E. Bodoki, V. Chis and C. M. Lucaciu, *Phys. Chem. Chem. Phys.*, 2015, **17**, 1281–1289.
51 R. G. Xiong, X. Z. You, B. F. Abrahams, Z. L. Xue and C. M. Che, *Angew. Chem., Int. Ed.*, 2001, **40**, 4422–4425.
52 P. Paik, A. Gedanken and Y. Mastai, *J. Mater. Chem.*, 2010, **20**, 4085–4093.
53 L. Yang, C. J. Chen, X. Liu, J. Shi, G. Wang, L. D. Zhu, L. P. Guo, J. D. Glennon, N. M. Scully and B. E. Doherty, *Electrophoresis*, 2010, **31**, 1697–1705.
54 N. Na, Y. P. Hu, J. Ouyang, W. R. G. Baeyens, J. R. Delanghe, Y. E. C. Taes, M. X. Xie, H. Y. Chen and Y. P. Yang, *Talanta*, 2006, **69**, 866–872.
55 A. Kühnle, T. R. Linderoth, B. Hammer and F. Besenbacher, *Nature*, 2002, **415**, 891–893.